

Bimetallic Cyanide-Bridged Coordination Polymers as Lithium Ion Cathode Materials: Core@Shell Nanoparticles with Enhanced Cyclability

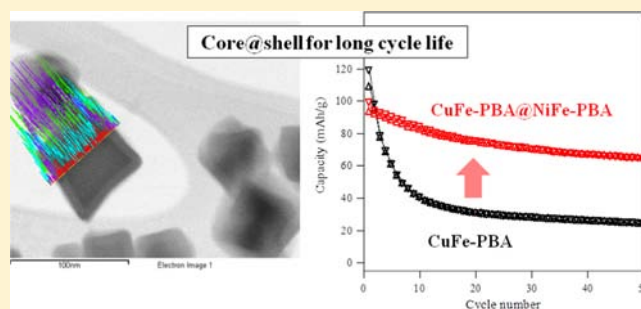
Daisuke Asakura,[†] Carissa H. Li,[‡] Yoshifumi Mizuno,[†] Masashi Okubo,^{*,†} Haoshen Zhou,[†] and Daniel R. Talham^{*,‡}

[†]National Institute of Advanced Industrial Science and Technology (AIST), Umezono 1-1-1, Tsukuba 305-8568, Japan

[‡]Department of Chemistry, University of Florida, Gainesville, Florida 32611-7200, United States

Supporting Information

ABSTRACT: Prussian blue analogues (PBAs) have recently been proposed as electrode materials for low-cost, long-cycle-life, and high-power batteries. However, high-capacity bimetallic examples show poor cycle stability due to surface instabilities of the reduced states. The present work demonstrates that, relative to single-component materials, higher capacity and longer cycle stability are achieved when using Prussian blue analogue core@shell particle heterostructures as the cathode material for Li-ion storage. Particle heterostructures with a size dispersion centered at 210 nm composed of a high-capacity $K_{0.1}Cu[Fe(CN)_6]_{0.7} \cdot 3.8H_2O$ (CuFe-PBA) core and lower capacity but highly stable shell of $K_{0.1}Ni[Fe(CN)_6]_{0.7} \cdot 4.1H_2O$ have been prepared and characterized. The heterostructures lead to the coexistence of both high capacity and long cycle stability because the shell protects the otherwise reactive surface of the highly reduced state of the CuFe-PBA core. Furthermore, interfacial coupling to the shell suppresses a known structural phase transition in the CuFe-PBA core, providing further evidence of synergy between the core and shell. The structure and chemical state of the heterostructure during electrochemical cycling have been monitored with ex situ X-ray diffraction and X-ray absorption experiments and compared to the behavior of the individual components.



INTRODUCTION

Electrochemical energy storage is a key element of sustainability efforts focused on power sources for electronic devices, transportation, and the power grid.¹ Li-ion batteries currently power most portable electronics, and larger-scale deployment is highly desired.^{2–4} Commercial Li-ion batteries include oxide ($LiCoO_2$, $LiMn_2O_4$, or $Li[NiCoAl]O_2$) or polyanion ($LiFePO_4$) cathodes,⁵ yet the development of new cathode materials remains one of the most important issues to be faced on the road to lower cost, safe, higher power, and higher energy content batteries.

Recently, Prussian blue analogues (PBAs) have been reported as promising cathode materials.^{6–11} PBAs have the general formula $A_xM'_k[M'(CN)_6]_l \square_m \cdot nH_2O$ (A, alkali metal; M, M', transition metal; \square , $[M'(CN)_6]$ vacancy; hereafter denoted as MM'-PBA),¹² with an open framework that provides highly reversible intercalation and extraction of ions with either aqueous or organic electrolytes.^{4,13} For example, Wessells et al. proposed application of PBAs as electrode materials in aqueous batteries.^{9,10} With a Na-ion aqueous electrolyte, NiFe-PBA allowed 66% retention of the capacity at extremely high rates (41.7 C).⁹ The reversible intercalation and extraction of Li ion with organic electrolytes are also important from the viewpoint of high energy, and it was shown that the

capacity of a NiFe-PBA with organic electrolytes does not fade over 100 cycles.¹⁴ However, most PBAs show only a one-electron-redox process of either the $M^{n+/(n+1)+}$ or $M'^{n+/(n+1)+}$ couple, which results in a small specific capacity of ca. 60 mAh/g.⁷ Thus, PBAs in which both metal ions are redox active are crucial for increased specific capacity. The CuFe-PBA with a Li-ion organic electrolyte, for example, shows two-electron charging and discharging involving both $Cu^{+2/+}$ and $Fe^{2+/3+}$ couples to give a specific capacity of about 120 mAh/g. Unfortunately, the capacity decreases with cycling due to instability of the reduced states.^{15,16}

A potentially effective strategy for enhancing the redox stability is to enclose the high-capacity PBAs in a core@shell structure with a robust shell, such as the well-characterized NiFe-PBA. The synergistic effects of a core@shell structure leading to the coexistence of both high capacity and good stability in a cathode material have been described for Ni-rich $Li[Ni_{1-x}M_x]O_2$.^{17–19} For example, the cycle stability of high-capacity Ni-rich $Li[Ni_{0.8}Co_{0.1}Mn_{0.1}]O_2$ can be drastically improved by adding a stable Mn-rich $Li[Ni_{0.5}Mn_{0.5}]O_2$ shell,

Received: December 13, 2012

Published: February 7, 2013

because part of the Mn does not participate in the charge/discharge redox process, stabilizing the oxide framework.¹⁷

To date, core@shell heterostructured PBAs have been developed mainly from the viewpoint of their magnetism.^{20–23}

The synthetic procedure reported by Brinzei et al. allows the epitaxial growth of successive layers of different PBAs to generate core@shell PBA particles.²² By adapting this procedure, we have targeted core@shell structures with a high-capacity CuFe-PBA core and a stable NiFe-PBA shell. Here, we report the synthesis of CuFe-PBA@NiFe-PBA and the synergistic effects of the heterostructure on the electrode properties, demonstrating that the core@shell structure improves cycle stability by stabilizing the surface of the cyanide framework and suppressing a charge-state-induced solid–solid phase transition in the core.

EXPERIMENTAL SECTION

All reagents were purchased from Sigma-Aldrich or Fisher-Acros and used without further purification. Deionized water used in synthetic procedures was obtained from a Barnstead NANOpure purification system. The filters used during the synthesis are Fast PES Bottle Top Filters with 0.45 μm pore size (Nalgene).

Core Particles (CuFe-PBA). The synthesis of the CuFe-PBA for core particles was performed at room temperature. A 100 mL aqueous solution of $\text{CuCl}_2 \cdot 2\text{H}_2\text{O}$ (4 mM) and an equal volume of an aqueous solution containing $\text{K}_3\text{Fe}(\text{CN})_6$ (4.7 mM) were simultaneously added dropwise to 200 mL of deionized water. The solution was vigorously stirred for 18 h after complete addition. The particles were subsequently filtered under vacuum using a 0.45 μm filter before being washed with nanopure water. The particles were again dispersed in water with sonication, collected, and washed for two additional cycles. The largest particles (>300 nm) were removed by centrifuge to improve the size distribution. For collection and analysis, the particles were redispersed in a 50/50 solvent mixture of water and acetone and dried under room temperature.

$\text{K}_{0.1}\text{Cu}[\text{Fe}(\text{CN})_6]_{0.7} \cdot 3.8\text{H}_2\text{O}$: 136 \pm 29 nm, yellow powder. IR (KBr): 2103 (s, ν_{CN} , $\text{Cu}^{\text{II}}-\text{NC}-\text{Fe}^{\text{III}}$); 2154 cm^{-1} (w, ν_{CN} , $\text{Cu}^{\text{II}}-\text{NC}-\text{Fe}^{\text{III}}$). EDS (K/Cu/Fe): 2.04/61.10/36.86. Weight % (K/Cu/Fe): 1.33/64.48/34.19. Anal. Calcd for $\text{C}_{4.2}\text{H}_{7.6}\text{N}_{4.2}\text{O}_{3.8}\text{K}_{0.1}\text{Cu}_{1.0}\text{Fe}_{0.7}$: C, 17.78; H, 2.66; N, 20.78; Cu, 22.39; Fe, 13.78. Found: C, 17.89; H, 2.66; N, 19.72; Cu, 22.9; Fe, 13.5.

Core@Shell Particles (CuFe-PBA@NiFe-PBA). The previously prepared core particles were dispersed in 400 mL of deionized water. A 200 mL aqueous solution of $\text{NiCl}_2 \cdot 6\text{H}_2\text{O}$ (3.8 mM) and an equal volume of an aqueous solution of $\text{K}_3\text{Fe}(\text{CN})_6$ (4.2 mM) were added using a peristaltic pump at a rate of 10 mL/h. Once the addition was complete, the particles were filtered using a 0.45 μm filter and washed with nanopure water. For isolation of the particles, they were dispersed in a 50/50 solvent mixture of water and acetone and dried at room temperature.

$\text{K}_{0.1}\text{Cu}[\text{Fe}(\text{CN})_6]_{0.7} \cdot 3.8\text{H}_2\text{O} @ \text{K}_{0.1}\text{Ni}[\text{Fe}(\text{CN})_6]_{0.7} \cdot 4.1\text{H}_2\text{O}$: 208 \pm 29 nm, yellow powder. IR (KBr): 2168 (w, ν_{CN} , $\text{Ni}^{\text{II}}-\text{NC}-\text{Fe}^{\text{III}}$); 2103 (s, ν_{CN} , $\text{Cu}^{\text{II}}-\text{NC}-\text{Fe}^{\text{III}}$); 2154 cm^{-1} (w, ν_{CN} , $\text{Cu}^{\text{II}}-\text{NC}-\text{Fe}^{\text{III}}$). EDS (K/Cu/Ni/Fe): 2.79/32.93/27.93/36.34; assuming the core composition has not changed gives (K/Cu/Fe) 1.08/32.93/19.85; (K/Ni/Fe) 1.71/27.93/16.49. Weight % (K/Cu/Fe): 0.75/35.64/18.89; (K/Ni/Fe) 1.11/27.93/15.81. Anal. Calcd for $\text{C}_{8.4}\text{H}_{15.8}\text{N}_{8.4}\text{O}_{7.9}\text{K}_{0.2}\text{Cu}_{1.0}\text{Ni}_{1.0}\text{Fe}_{1.4}$: C, 17.74; H, 2.82; N, 20.70; Cu, 11.18; Ni, 10.31; Fe, 13.75. Found: C, 17.65; H, 2.82; N, 19.68; Cu, 11.2; Ni, 10.1; Fe, 13.4.

Instrumentation. Infrared spectra were recorded on a Nicolet 6700 Thermo Scientific spectrophotometer. Typically 16 scans were taken between 2300 and 1900 cm^{-1} with a precision of 0.482 cm^{-1} . Powder samples were mixed with KBr and pressed into a pellet using 4000 psi. A scan of pure KBr was taken as a background reference. The chemical composition was determined by the standard microanalytical method (CE Instruments, EA1110) for the elements C, H, and N and by inductively coupled plasma atomic emission spectroscopy (ICP-

AES, SII nanotechnology, SPS4000) for Fe, Ni, and Cu. Transmission electron microscopy (TEM) was performed on a JEOL-2010F HRTEM at 200 kV. The TEM grids (ultrathin carbon film on holey carbon support film, 300 mesh, gold from Ted-Pella, Inc.) were prepared by dropping, onto the grid, 40 μL of a solution containing 5 mg of sample dispersed by sonication in 1 mL of water for 30 min. Energy dispersive X-ray spectroscopy (EDX) was performed with an Oxford Instruments EDS X-ray Microanalysis System coupled to the HRTEM microscope. A total of three scans were performed on different parts of the sample and then averaged to give relative atomic percentages for potassium, copper, iron, and nickel. Also, an EDX linescan was performed on potassium, copper, iron, and nickel in order to see the core@shell structure of the particles.

Electrochemical Experiments. Electrochemical intercalation and deintercalation of Li ions were performed by using a three-electrode glass cell, in which lithium metal was employed as counter and reference electrodes. Each core or core@shell sample (50 mg) was ground with acetylene black (13.3 mg) and polytetrafluoroethylene (PTFE) into a paste and used as the working electrode. For the electrolyte, 1 M LiClO_4 ethylene carbonate (EC)–diethyl carbonate (DEC) solution (1/1 v/v %) was used. The cutoff voltages were 2.5 V (vs Li/Li^+) for Li-ion insertion and 4.3 V for Li-ion extraction. Quantitative Li-ion insertion/extraction was carried out by the galvanostatic intermittent titration technique (GITT), in which a low-density current was repeatedly applied for 10 min followed by an interruption of 30 min. Powder X-ray diffraction was carried out on a Rigaku SmartLab instrument using $\text{Cu K}\alpha$ radiation in steps of 0.01° over the 2θ range of 30–60°. The unit cell parameters were calculated by least-squares fitting. The ex situ XRD patterns were recorded after washing the lithiated and delithiated samples with ethanol.

X-ray Absorption Spectroscopy. X-ray absorption near-edge structure (XANES) measurements were performed using synchrotron radiation on beamline BL-7C of the Photon Factory. The quantitatively lithiated/delithiated samples were prepared by the GITT, washed with ethanol, and then dried in vacuo. The spectra were recorded in the transmission mode at room temperature under an ambient atmosphere. The X-ray energy for each edge was calibrated by using the corresponding metal foil. The obtained experimental data were analyzed using Rigaku REX2000 software.

RESULTS

A TEM image of the cubic CuFe-PBA particles appears in Figure 1a, and the measured size dispersion, centered near 135 nm, is presented in Figure 2a. The core@shell particles were prepared by starting with a suspension of the CuFe-PBA and

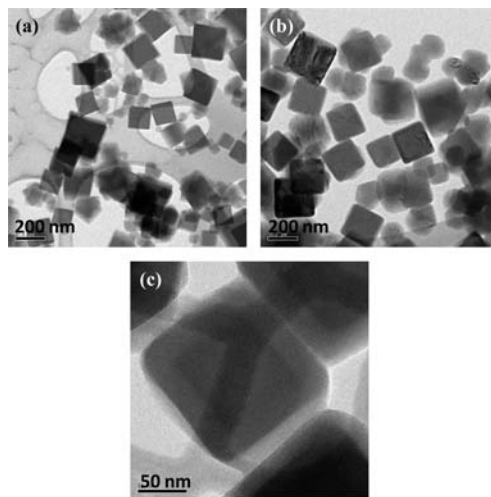


Figure 1. HRTEM images of (a) the CuFe-PBA core and (b, c) the CuFe-PBA@NiFe-PBA core@shell particles.

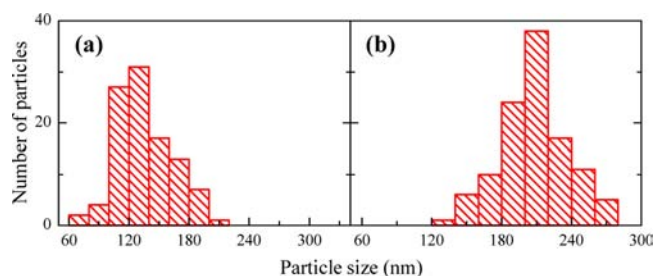


Figure 2. Size distributions of (a) the CuFe-PBA core particles and (b) the CuFe-PBA@NiFe-PBA particles. For both samples more than 100 particles were measured, taken from pictures of different areas on the TEM grid, using ImageJ software. The average sizes and standard deviations are 136 ± 29 nm for the uncoated particles and 208 ± 29 nm for the core@shell particles.

growing $K_xNi[Fe(CN)_6]_k \cdot nH_2O$ under conditions that favor heterogeneous precipitation, as previously described for other core@shell PBAs.^{20–23} The core@shell size dispersion is centered near 210 nm (Figure 2b), and TEM images reveal a uniform coating of the CuFe-PBA core by the NiFe-PBA shell (Figure 1b,c). Powder X-ray diffraction and chemical analysis using EDX support the core@shell architecture anticipated by the fabrication sequence. The room-temperature XRD pattern (vide infra) can be assigned to two separate cubic PBA lattices with the unit cell parameters $a = 10.158$ Å for CuFe-PBA and $a = 10.239$ Å for NiFe-PBA, indicating segregation of the two materials with little mixing of the M^{2+} ions.^{14,16}

The cyanide stretching frequencies measured by FTIR (Figure S1, Supporting Information) are also consistent with the presence of both CuFe-PBA and NiFe-PBA lattices.^{16,21} Likewise, EDX line scans (Figure 3) show localization of the

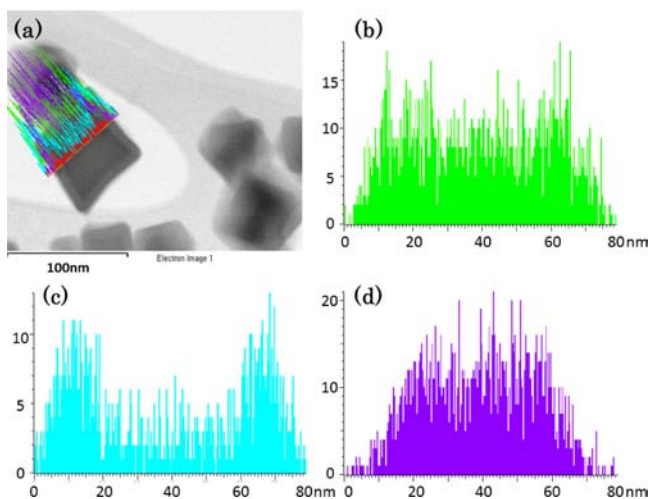


Figure 3. EDX line scans and the corresponding TEM image (a) of a CuFe-PBA@NiFe-PBA particle for iron (b), nickel (c), and copper (d). Data are counts for each element detected against the position of the electron beam along the line in the figure shown on the left.

Ni^{2+} ions at the edges of the particle with Cu^{2+} in the core. The average formula unit of the CuFe-PBA@NiFe-PBA is determined as $K_{0.1}Cu_{0.5}Ni_{0.5}[Fe(CN)_6]_{0.7} \cdot 3.95H_2O$ ($K_{0.1}Cu[Fe(CN)_6]_{0.7} \cdot 3.8H_2O @ K_{0.1}Ni[Fe(CN)_6]_{0.7} \cdot 4.1H_2O$) on the basis of the elemental analysis.

Cyclic voltammetric scans of the CuFe-PBA and CuFe-PBA@NiFe-PBA particle electrodes as pastes of acetylene black

and PTFE are compared in Figure 4. The electrolytic medium is 1 M $LiClO_4/EC-DEC$, and the scan rate is 0.1 mV/s. The

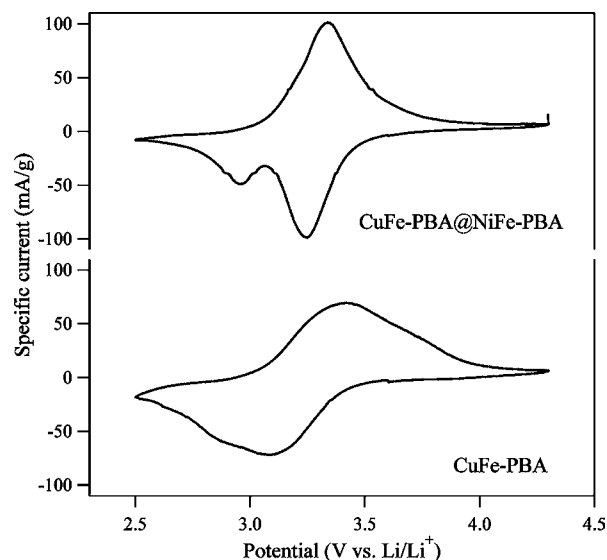


Figure 4. Cyclic voltammograms for the uncoated CuFe-PBA and the CuFe-PBA@NiFe-PBA core@shell particles with 1 M $LiClO_4/EC-DEC$. The sweep rate was 0.1 mV/s.

CuFe-PBA particles show a broad cathodic peak around 3.09 V vs Li/Li^+ with a small shoulder at 2.86 V, corresponding to the Li-ion insertion steps. For the anodic scan, a broad peak is observed around 3.41 V vs Li/Li^+ , also containing a shoulder, suggesting multiple processes. The peak-to-peak separation, ΔE_p , is 320 mV, much larger than that expected for a one-step, one-electron, reversible reaction at a sufficiently slow scan rate.²⁴ The observation is consistent with a previous study which demonstrated that the CuFe-PBA framework exhibits two separate redox processes, one corresponding to the Fe^{3+}/Fe^{2+} couple and the other to the Cu^{2+}/Cu^+ couple, with poor reversibility attributed to a structural phase transition in the highly reduced state along with surface decomposition.¹⁶ Therefore, the large ΔE_p value in the CV curve for the CuFe-PBA particles can be attributed to the irreversibility of the electrode reaction.

In contrast, the CV curve for the core@shell particles exhibits a sharp cathodic peak around 3.24 V vs Li/Li^+ with a smaller, well-defined cathodic peak around 2.95 V vs Li/Li^+ . The larger 3.24 V peak is attributable to Fe^{3+} reduction, while the smaller 2.95 V peak is associated with Cu^{2+} reduction, on the basis of the standard electrode potentials of 0.36 V vs NHE (3.40 V vs Li/Li^+) for the $[Fe(CN)_6]^{3-/4-}$ couple and 0.16 V vs NHE (3.20 V vs Li/Li^+) for the $Cu^{2+/+}$ couple.²⁴ The anodic peak at 3.33 V vs Li/Li^+ again contains multiple components, although it is not as well resolved as for the cathodic scan. It is nevertheless much sharper than for the uncoated CuFe-PBA particles, despite the presence of two different PBAs in the core@shell particles. The peak-to-peak separation between the anodic and cathodic main peaks is just 90 mV, indicating a faster and more reversible electrode process than for the uncoated particles. The clear difference between the CV curves for the coated and uncoated particles can be ascribed to the core@shell structure. The surface decomposition previously observed for CuFe-PBA upon redox cycling is suppressed by

the stable NiFe-PBA shell protecting the surface, in which Ni²⁺ reduction does not occur.

Charge–discharge curves at a constant specific current of 10 mA/g are shown in Figure 5. The initial discharge capacity for

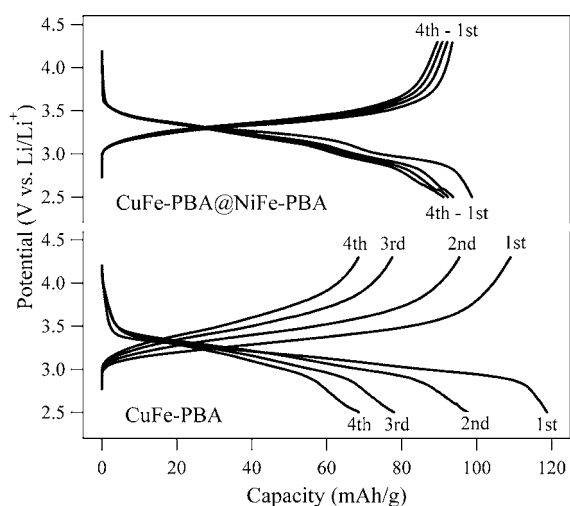


Figure 5. Charge–discharge curves for the uncoated CuFe-PBA and the CuFe-PBA@NiFe-PBA core@shell particles at a constant specific current of 10 mA/g.

the uncoated CuFe-PBA particles reached 119 mAh/g. This capacity corresponds to 1.2 Li⁺ ions per formula unit of K_{0.1}Cu[Fe(CN)₆]_{0.7}·3.8H₂O, which exceeds the number of moles (0.7) of [Fe(CN)₆]^{3-/4-} and corresponds to 0.5 Li⁺ associated with the Cu^{2+/+} couple. Thus, the large capacity for CuFe-PBA can be attributed to the partial redox of Cu²⁺ as well as the [Fe(CN)₆]³⁻. However, as shown in Figure 6, the available capacity fades rapidly with cycling of the charge–discharge process. The remaining capacity after 50 charge–discharge cycles was only 21% of the initial capacity.

The initial discharge capacity for the core@shell particles is 99 mAh/g, smaller than that for the uncoated particles because Ni²⁺ in the NiFe-PBA shell is not reduced. However, the capacity again corresponds to one Li-ion per [Fe(CN)₆]^{3-/4-} in both the CuFe-PBA core and the NiFe-PBA shell, plus 0.6 Li⁺

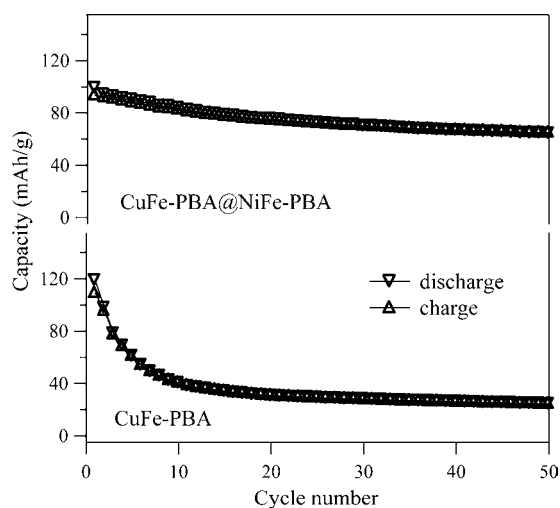


Figure 6. Cycle stability of the uncoated CuFe-PBA and the CuFe-PBA@NiFe-PBA core@shell particles.

per Cu^{2+/+} site in the core. These assignments are consistent with the relative magnitudes of the resolved cathodic peaks in the CV. On the other hand, the cycle stability of the core@shell particles is much better than that of the uncoated CuFe-PBA. The remaining capacity after 50 charge–discharge cycles is 65% of the initial capacity. The improved cycle stability of the core@shell particles should be attributable to the protective effect of the NiFe-PBA shell, which is stable against the surface decomposition previously observed for CuFe-PBA.¹⁶

Structural changes of the core@shell particles upon redox cycling and Li⁺ intercalation were followed with ex situ powder XRD (Figure 7). Peaks associated with both the NiFe-PBA and

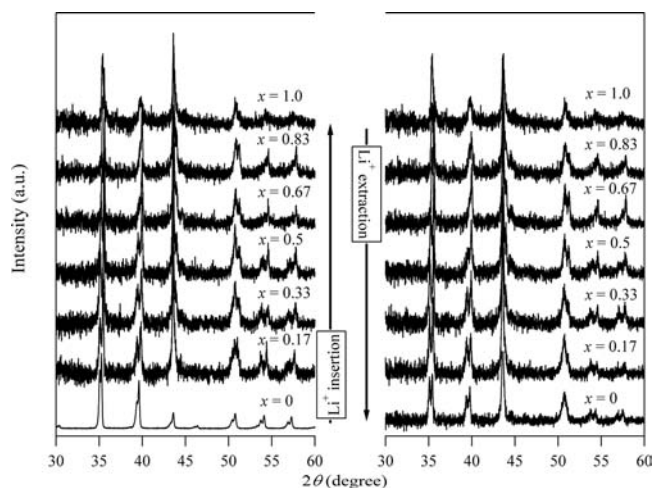


Figure 7. Ex situ X-ray diffraction patterns for Li_x(CuFe-PBA@NiFe-PBA) during Li-ion insertion and extraction (0 < x < 1.0).

the CuFe-PBA components shift gradually upon cycling, and no additional peaks appear. The gradual shifts suggest that the Li-ion insertion/extraction proceeds homogeneously through a solid solution process and not through formation of heterogeneous domains of the different redox states.

In Figure 8, the unit cell parameter, *a*, for the CuFe-PBA core and NiFe-PBA shell, determined from the XRD pattern in Figure 7, are plotted vs Li-ion incorporation, *x*, in Li_x(CuFe-PBA@NiFe-PBA). For reference, the open circuit voltages (OCVs) associated with each sample are also plotted. For the NiFe-PBA shell, *a* monotonically decreases from 10.239 Å (*x* = 0) to 10.159 Å (*x* = 0.64) upon inserting Li ion and then remains essentially constant for 0.7 < *x* < 1.0. The change in *a* is reversible with Li-ion extraction. The monotonic change in *a* for 0 < *x* < 0.7 is consistent with results for single-phase samples of Li_x(NiFe-PBA) (Figure S2, Supporting Information), suggesting that Li-ion insertion/extraction for the NiFe-PBA shell in Li_x(CuFe-PBA@NiFe-PBA) occurs only for 0 < *x* < 0.7. The NiFe-PBA is highly stable over many Li-ion insertion/extraction cycles.¹⁴

For the CuFe-PBA core, *a* decreases from 10.158 Å (*x* = 0) to 10.075 Å (*x* = 0.64) and then slightly increases to 10.091 Å (*x* = 0.98). The change in *a* is also reversed during the Li-ion extraction. Loadings greater than *x* = 0.7 result from Cu²⁺ reduction, and the core@shell behavior is significantly different from that previously observed for uncoated particles (Figure S3, Supporting Information), for which higher Li-ion loadings (*x* > 0.7 for Li_x(CuFe-PBA)) were accompanied by a cubic to tetragonal structural phase transition.¹⁶ On cycling as part of

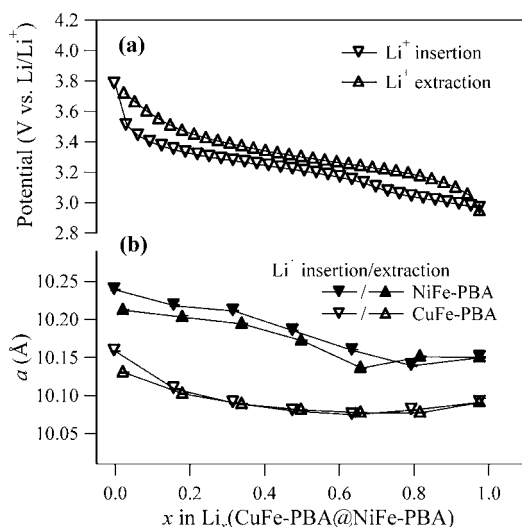


Figure 8. (a) Open circuit voltages for CuFe-PBA@NiFe-PBA during Li-ion insertion and extraction. (b) Unit cell parameters for the NiFe-PBA shell and CuFe-PBA core in $\text{Li}_x(\text{CuFe-PBA@NiFe-PBA})$ during Li-ion insertion and extraction.

the core@shell architecture, no structural phase transition is observed.

To confirm the electronic changes during Li-ion insertion/extraction, the X-ray absorption near edge structure (XANES) spectra were recorded. Previous studies on CuFe-PBA and NiFe-PBA have already confirmed the reversible reduction of Fe^{3+} .^{14,16} Figure 9 reports the Fe and Cu K-edge XANES of the core@shell particles during Li-ion insertion and extraction. The Ni K-edge XANES is shown in Figure S4 (Supporting Information). As expected from the cyclic voltammetry and charge/discharge curves, there is no change in the Ni^{2+} oxidation state. For $0 < x < 0.7$, the Fe K-edge XANES shows the reversible shift of the most intense peak between 7125.9 to 7124.9 eV, while no peak shift is observed for $0.7 < x < 1.0$. On the other hand, although there is no change in the Cu^{2+} oxidation state for $0 < x < 0.7$, XANES provides clear evidence of Cu^{2+} reduction upon Li-ion insertion greater than $x = 0.7$, with the emergence of the peak at 8980.3 eV corresponding to the reduction of Cu^{2+} to Cu^+ .²⁵ After Li-ion extraction ($x = 0$), the reduced state peak almost disappears and the initial peak at 8983.4 eV, characteristic of Cu^{2+} , again becomes more intense. The reversibility of the change in the Cu K-edge XANES for the core@shell particles upon charge/discharge is much better than that for the uncoated CuFe-PBA (Figure S5, Supporting Information), which explains the improved cycle stability of the core@shell PBA electrode. However, it should also be pointed out that the reduced state peak, at 8980.3 eV after Li-ion extraction, does not completely disappear upon reoxidation, indicating some “trapped” Cu^+ . The XANES is consistent with the initial coulombic efficiency that shows a slight decrease in the charge capacity in comparison to the discharge capacity at the first cycle. It is expected that the completely oxidized shell will be a poor ion conductor; thus, if the kinetics of shell and core oxidation are not perfectly matched, some charge might be “trapped” in the core. It is important to note, though, that the structural change associated with Cu^{2+} reduction that was seen in the uncoated CuFe-PBA particles is not observed in the core@shell particles; thus, the incomplete reversal of the copper redox process has different origins in the uncoated and coated particles.

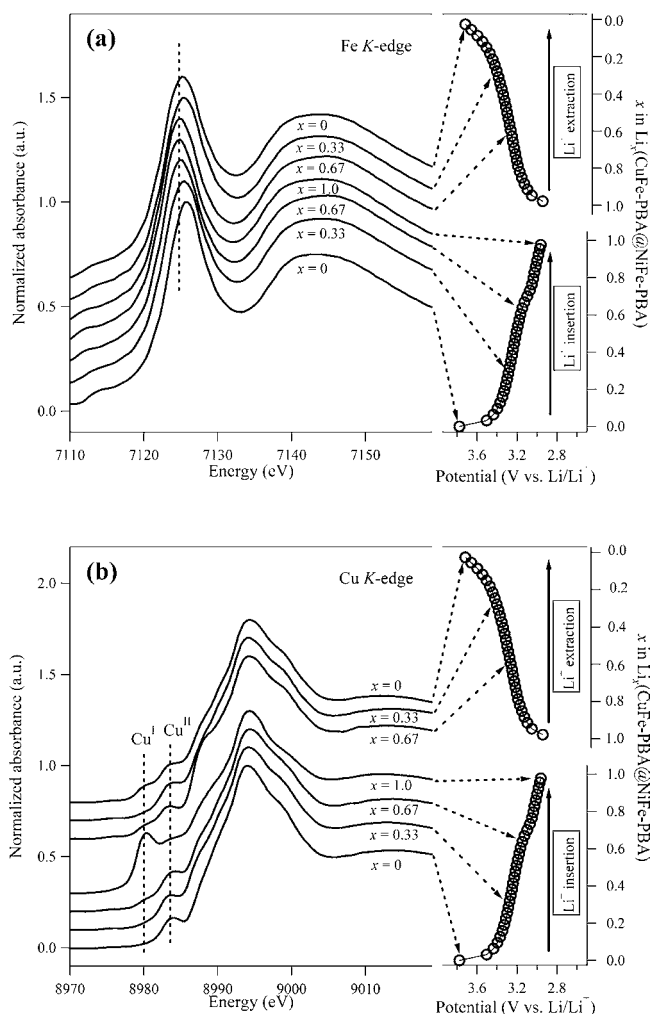
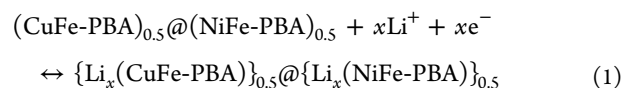


Figure 9. (a) Fe K-edge and (b) Cu K-edge XANES spectra for $\text{Li}_x(\text{CuFe-PBA@NiFe-PBA})$.

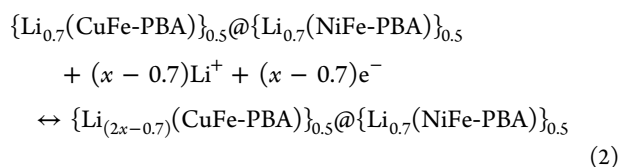
DISCUSSION

The initial measured capacity of the core@shell particles of 99 mAh/g is less than the 119 mAh/g of the uncoated CuFe-PBA particles because the redox inactivity of Ni^{2+} limits the capacity of the shell to one charge per formula unit. Nevertheless, the lower initial capacity is offset by the significantly enhanced cycle stability. The charge/discharge curves, cyclic voltammetry, and ex situ XRD analyses are all consistent with the concurrent and homogeneous reduction and oxidation of the $\text{Fe}^{2+/3+}$ sites in both the core CuFe-PBA and the shell NiFe-PBA, up to $x = 0.7$, which corresponds to the $[\text{Fe}(\text{CN})_6]^{4-/3-}$ content in both core and shell as determined by the compound stoichiometry. Beyond $x = 0.7$, the $\text{Cu}^{2+/+}$ couple is accessed up to $x = 1.0$. The charging of the Cu^{2+} sites corresponds to $\sim 0.6e$ per copper site, very similar to the $\sim 0.5e$ per site observed for the uncoated CuFe-PBA (Figure 5).

The Li-ion insertion/extraction for the core@shell particles, $\text{Li}_x(\text{CuFe-PBA@NiFe-PBA})$, can be written as



for $0 < x < 0.7$ and then



for $0.7 < x < 1.0$. The expected fully lithiated state is $\{\text{Li}_{1.3}\text{K}_{0.1}\text{Cu}[\text{Fe}(\text{CN})_6]_{0.7} \cdot 3.8\text{H}_2\text{O}\}_{0.5} @ \{\text{Li}_{0.7}\text{K}_{0.1}\text{Ni}[\text{Fe}(\text{CN})_6]_{0.7} \cdot 4.1\text{H}_2\text{O}\}_{0.5}$, or $\text{Li}_{1.0}(\text{CuFe-PBA} @ \text{NiFe-PBA})$ when the core and shell components are in equal proportions.

The response of the highly lithiated core in the $\text{Li}_{1.0}(\text{CuFe-PBA} @ \text{NiFe-PBA})$ core@shell particles can be compared to that of the uncoated $\text{Li}_{1.2}(\text{CuFe-PBA})$ particles. In both cases, the extent of copper reduction is approximately the same, $\sim 0.5\text{e}$ per copper ion in the uncoated particles and $\sim 0.6\text{e}$ per ion in the core@shell particles. Figure 10 compares the ex situ XRD

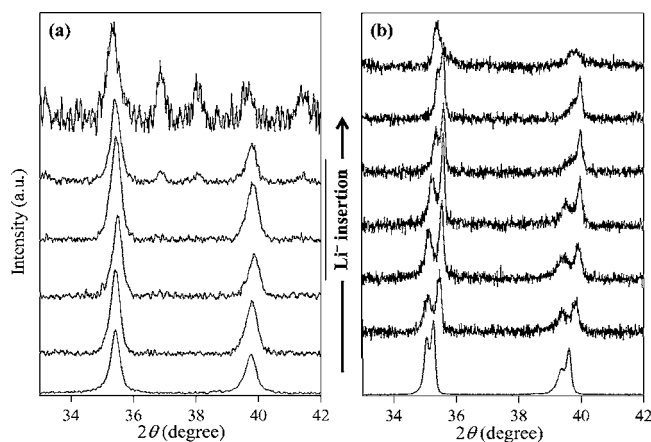


Figure 10. Ex situ XRD patterns, focusing on the (400) and (420) peaks of the original cubic structure, for (a) $\text{Li}_x(\text{CuFe-PBA})$ during Li-ion insertion ($0 < x < 1.2$) and (b) $\text{Li}_x(\text{CuFe-PBA} @ \text{NiFe-PBA})$ during Li-ion insertion ($0 < x < 1.0$).

patterns for the two cases, focusing on the original (400) and (420) peaks of the starting cubic phases. With increasing lithium loading, new peaks are observed for the uncoated particles, corresponding to the cubic to tetragonal phase transition,¹⁶ but are absent for the core@shell particles.

The change in the cubic unit cell parameter, a , of the uncoated particles, $\text{Li}_x(\text{CuFe-PBA})$, upon lithiation is plotted in Figure S3 (Supporting Information), which can be compared to the similar plot for the core@shell particles in Figure 8. The x dependence of a for $x < 1.0$ is almost the same as that for the CuFe-PBA core in $\text{Li}_x(\text{CuFe-PBA} @ \text{NiFe-PBA})$. However, for $x > 1.0$, a for $\text{Li}_x(\text{CuFe-PBA})$ drastically increases to 10.161 \AA as the phase change progresses. The emergence of a new phase and the drastic change in a for $x > 1.0$ should generate mechanical strain within the PBA particle, leading to reduced electrochemical reversibility and rapidly decreasing capacity of the uncoated particles. The similar extent of copper reduction in the core@shell particles should also be enough to induce the phase change, but it is not observed. The relatively inert $\text{Li}_{0.7}(\text{NiFe-PBA})$ shell stabilizes the overlithiated $\text{Li}_x(\text{CuFe-PBA})$ core, although at this point its role is not completely understood. Certainly, the shell protects the reactive surface of the highly lithiated core from irreversible reactions with the electrolytic medium. Alternatively, or in parallel, the coupling of the shell to the core may also add a barrier to the structural phase change. The NiFe-PBA would resist the tetragonal

distortion, and the potential strain at the cubic/tetragonal interface may provide a kinetic barrier to the phase change in the core.

The core@shell particles exhibit faster electrode kinetics in the cyclic voltammogram than do the uncoated CuFe-PBA particles, despite the larger size of the core@shell particles. The cathodic wave at 3.24 V vs Li/Li^+ corresponds to the simultaneous reduction of $[\text{Fe}(\text{CN})_6]^{3-}$ in both the NiFe-PBA shell and the CuFe-PBA core. The ferrocyanide oxidation of the core and shell again overlap in the anodic wave at 3.33 V vs Li/Li^+ , and the relatively small ΔE_p of 90 mV indicates a high level of reversibility for the $[\text{Fe}(\text{CN})_6]^{3-/4-}$ process, limited primarily by ion diffusion in the solid. On the other hand, although the Cu^{2+} reduction wave is nicely defined in the cathodic sweep at 2.95 eV vs Li/Li^+ , the oxidation wave is well separated from the reduction and is shifted into the $\text{Fe}^{2+/3+}$ wave.

Possible reasons for the lack of reversibility of the $\text{Cu}^{2+/+}$ couple could include a chemical or structural change at the copper ion. Unlike for the uncoated CuFe-PBA , which undergoes a cubic to tetragonal distortion, no structural change is seen when the core CuFe-PBA is surrounded by the NiFe-PBA shell. However, local changes in the Cu^+ coordination environment cannot be ruled out. It is interesting that the Cu^+ oxidation moves into the $[\text{Fe}(\text{CN})_6]^{4-}$ oxidation wave, which could reflect charge trapping in the CuFe-PBA core, requiring mixed valency in the surrounding NiFe-PBA for efficient electron and ion transport. The rectification behavior may also arise from the potential gradient of the core@shell particle.

Similarly, there is evidence of incomplete charge cycling of the core, which may also have kinetic origins associated with transport through the shell. Comparison of the XANES of the charged and discharged states (Figure 9) reveals remnant Cu^+ in the core after oxidation and release of Li^+ ions. Reduced capacity after the first several charge/discharge cycles (Figure 5) is consistent with incomplete redox of the core. If $[\text{Fe}(\text{CN})_6]^{3-/4-}$ electron exchange is fast relative to Cu^+ oxidation, the shell may achieve its fully oxidized state, which is also expected to be a poorer conductor, before Cu^+ oxidation is complete.

Finally, the sample capacity measured in the charge-discharge curves and the elemental content determined from elemental analysis are consistent with a core/shell ratio of ~ 1 in the samples prepared for this study. The $1/1$ core/shell ratio is in apparent discrepancy with the ratios inferred on the basis of the average particle sizes determined from the dispersions displayed in Figure 2. For the average or smaller particles, the shell volume is significantly larger than the core. However, for the larger particles, the situation is reversed. Figure 2 reports number averages, but the smaller number of larger particles dominate the sample mass because of the d^3 dependence. In these and other Prussian blue analogue core@shell particles, shell growth is faster on the smaller particles and shell thickness tends to be smaller on the larger particles in a polydisperse sample.²⁶ The $1/1$ molar ratios observed in the bulk measurements are a consequence of the rather wide range of particle sizes isolated when preparing the CuFe-PBA core. Although not quantified, the FTIR spectra and XRD patterns also qualitatively agree with a $1/1$ ratio of CuFe-PBA to NiCr-PBA . The spread in core/shell ratios in the present samples suggests that there is opportunity to improve the charging capacity as the optimum shell thickness is determined and

synthetic methods are improved to achieve narrower particle size dispersions.

CONCLUSIONS

The study demonstrates that the use of core@shell heterostructures represents a viable strategy for improving the performance of coordination polymer ion storage materials and opens new perspectives that are not accessible to the conventional electrode materials. A stable shell material that allows ion transport to a high-capacity core can protect the core from irreversible surface reactions at the extremes of charging and discharging that degrade performance. If the shell is electroactive, it can also contribute to the storage capacity. In the example demonstrated here, the CuFe-PBA undergoes reversible charging and discharging, with the NiFe-PBA shell facilitating transport of ions to the core and at the same time contributing to the storage capacity, albeit at a lesser extent than the core.

Another important characteristic of the core@shell heterostructure is the interfacial coupling of the two components. Previous studies of coordination polymer heterostructures demonstrated that stress coupling across an interface allows structural changes in one component to be reflected in the structural and physical properties of the other.²¹ In the present case, the interface between the materials suppresses a structural phase transition normally experienced by the single-phase material, here the cubic to tetragonal transition of the CuFe-PBA in the overlithiated state.

ASSOCIATED CONTENT

Supporting Information

Figures giving IR spectra, unit cell parameters of $\text{Li}_x(\text{NiFe-PBA})$ and $\text{Li}_x(\text{CuFe-PBA})$, Ni K-edge XANES of $\text{Li}_x(\text{CuFe-PBA@NiFe-PBA})$, and Cu K-edge XANES of $\text{Li}_x(\text{CuFe-PBA})$. This material is available free of charge via the Internet at <http://pubs.acs.org>.

AUTHOR INFORMATION

Corresponding Author

*E-mail: m-okubo@aist.go.jp (M.O.); talham@chem.ufl.edu (D.R.T.).

Notes

The authors declare no competing financial interest.

ACKNOWLEDGMENTS

Part of this work was financially supported by Industrial Technology Research Grant Program in 2010 from the New Energy and Industrial Development Organization (NEDO). M.O. was supported by a KAKENHI on Innovative Areas ("Coordination Programming" Area 2107) from MEXT, Japan. Support by the U.S. National Science Foundation through grant DMR-1005581 (D.R.T.) is gratefully acknowledged. The X-ray absorption spectroscopy was done under the approval of the Photon Factory Program Advisory Committee (Proposal No. 2012G110). Finally, we acknowledge helpful insights by anonymous reviewers.

REFERENCES

- (1) Dunn, B.; Kamath, H.; Tarascon, J. M. *Science* **2011**, *334*, 928–935.
- (2) Goodenough, J. B. *J. Solid State Electrochem.* **2012**, *16*, 2019–2029.

- (3) Etacheri, V.; Marom, R.; Elazari, R.; Salitra, G.; Aurbach, D. *Energ. Environ. Sci.* **2011**, *4*, 3243–3262.
- (4) Huggins, R. A. *Advanced Batteries*; Springer: Berlin, 2009.
- (5) Nazri, G. A.; Pistoia, G. *Lithium Batteries*; Springer: Berlin, 2009.
- (6) Okubo, M.; Asakura, D.; Mizuno, Y.; Kim, J. D.; Kudo, T.; Honma, I. *J. Phys. Chem. Lett.* **2010**, *1*, 2063–2071.
- (7) (a) Asakura, D.; Okubo, M.; Mizuno, Y.; Kudo, T.; Zhou, H. S.; Amemiya, K.; de Groot, F. M. F.; Chen, J. L.; Wang, W. C.; Glans, P. A.; Chang, C.; Guo, J.; Honma, I. *Phys. Rev. B* **2011**, *84*, 045117. (b) Nanba, Y.; Asakura, D.; Okubo, M.; Mizuno, Y.; Kudo, T.; Zhou, H.; Amemiya, K.; Guo, J.; Okada, K. *J. Phys. Chem. C* **2012**, *116*, 24896–24901.
- (8) Mizuno, Y.; Okubo, M.; Asakura, D.; Saito, T.; Hosono, E.; Saito, Y.; Oh-ishi, K.; Kudo, T.; Zhou, H. S. *Electrochim. Acta* **2012**, *63*, 139–145.
- (9) (a) Wessells, C. D.; Huggins, R. A.; Cui, Y. *Nat. Commun.* **2011**, *2*, 550. (b) Wessells, C. D.; Peddada, S. V.; Huggins, R. A.; Cui, Y. *Nano Lett.* **2011**, *11*, 5421–5425. (c) Wessells, C. D.; Peddada, S. V.; McDowell, M. T.; Huggins, R. A.; Cui, Y. *J. Electrochem. Soc.* **2012**, *159*, A98–103. (d) Wessells, C. D.; McDowell, M. T.; Peddada, S. V.; Pasta, M.; Huggins, R. A.; Cui, Y. *ACS Nano* **2012**, *6*, 1688–1694.
- (10) Pasta, M.; Wessells, C. D.; Huggins, R. A.; Cui, Y. *Nat. Commun.* **2012**, *3*, 1149.
- (11) Lu, Y.; Wang, L.; Cheng, J.; Goodenough, J. B. *Chem. Commun.* **2012**, *48*, 6544–6546.
- (12) Verdaguier, M.; Girolami, G. S. Magnetic Prussian blue analogs. In *Magnetism: Molecules to Materials V*; Miller, J. S., Dorillon, M., Eds.; Wiley-VCH: Weinheim, Germany, 2005.
- (13) Itaya, K.; Uchida, I. *Acc. Chem. Res.* **1986**, *19*, 162–168.
- (14) Mizuno, Y.; Okubo, M.; Kagesawa, K.; Asakura, D.; Kudo, T.; Zhou, H. S.; Oh-ishi, K.; Okazawa, A.; Kojima, N. *Inorg. Chem.* **2012**, *51*, 10311–10316.
- (15) Imanishi, N.; Morikawa, T.; Kondo, J.; Yamane, R.; Takeda, Y.; Yamamoto, O.; Sakaebe, H.; Tabuchi, M. *J. Power Sources* **1999**, *81*, 530–534.
- (16) Okubo, M.; Asakura, D.; Mizuno, Y.; Kudo, T.; Zhou, H. S.; Okazawa, A.; Kojima, N.; Ikeno, K.; Mizokawa, T.; Honma, I. *Angew. Chem., Int. Ed.* **2011**, *50*, 6269–6273.
- (17) Sun, Y. K.; Myung, S. T.; Kim, M. H.; Prakash, J.; Amine, K. *J. Am. Chem. Soc.* **2005**, *127*, 13411–13418.
- (18) Sun, Y. K.; Myung, S. T.; Park, B. C.; Prakash, J.; Belharouak, I.; Amine, K. *Nat. Mater.* **2009**, *8*, 320–324.
- (19) Sun, Y. K.; Chen, Z.; Noh, H. J.; Lee, D. J.; Jung, H. G.; Ren, Y.; Wang, S.; Yoon, C. S.; Myung, S. T.; Amine, K. *Nat. Mater.* **2012**, *11*, 942–947.
- (20) Catala, L.; Brinzei, D.; Prado, Y.; Gloter, A.; Stephan, O.; Rogez, G.; Mallah, T. *Angew. Chem., Int. Ed.* **2009**, *48*, 183–187.
- (21) Dumont, M. F.; Knowles, E. S.; Guiet, A.; Pajerowski, D. M.; Gomez, A.; Kycia, S. W.; Meisel, M. W.; Talham, D. R. *Inorg. Chem.* **2011**, *50*, 4295–4300.
- (22) Brinzei, D.; Catala, L.; Louvain, N.; Rogez, G.; Stephan, O.; Gloter, A.; Mallah, T. *J. Mater. Chem.* **2006**, *16*, 2593–2599.
- (23) Prado, Y.; Dia, N.; Lisnard, L.; Rogez, G.; Brisset, F.; Catala, L.; Mallah, T. *Chem. Commun.* **2012**, *48*, 11455–11457.
- (24) Bard, A. J.; Faulkner, L. R. *Electrochemical Methods*; Wiley: New York, 2001.
- (25) Ma, X. D.; Yokoyama, T.; Hozumi, T.; Hashimoto, K.; Ohkoshi, S. *Phys. Rev. B* **2005**, *72*, 094107.
- (26) Risset, O. N.; Knowles, E. S.; Ma, S.; Meisel, M. W.; Talham, D. R. *Chem. Mater.* **2013**, *25*, 42–47.